LANGMUIR

Article

pubs.acs.org/Langmuir

Effect of Nanoclustering and Dipolar Interactions in Heat Generation for Magnetic Hyperthermia

Diego F. Coral,[†] Pedro Mendoza Zélis,[†] Marzia Marciello,[‡] María del Puerto Morales,[‡] Aldo Craievich,[§] Francisco H. Sánchez,[†] and Marcela B. Fernández van Raap*[,†]

[†]Physics Department, Physics Institute of La Plata (IFLP- CONICET), Faculty of Exact Sciences, National University of La Plata, c.c. 67, 1900 La Plata, Argentina

[‡]Department of Biomaterials and Bioinspired Materials, Materials Science Institute of Madrid (ICMM)/CSIC, Sor Juana Inés de la Cruz 3, Cantoblanco, 28049 Madrid, Spain

[§]Institute of Physics, University of Sao Paulo, C.P. 66318 Sao Paulo SP, Brazil

Supporting Information

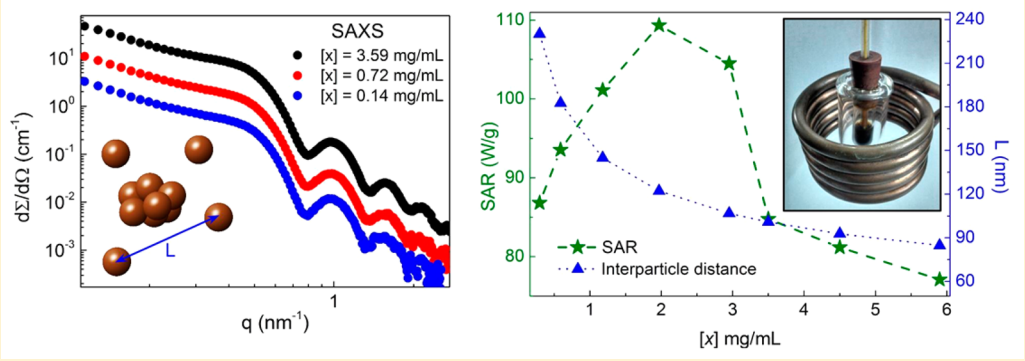

ABSTRACT: Biomedical magnetic colloids commonly used in magnetic hyperthermia experiments often display a bidisperse structure, i.e., are composed of stable nanoclusters coexisting with well-dispersed nanoparticles. However, the influence of nanoclusters in the optimization of colloids for heat dissipation is usually excluded. In this work, bidisperse colloids are used to analyze the effect of nanoclustering and long-range magnetic dipolar interaction on the magnetic hyperthermia efficiency. Two kinds of colloids, composed of magnetite cores with mean sizes of around 10 and 18 nm, coated with oleic acid and dispersed in hexane, and coated with meso-2,3-dimercaptosuccinic acid and dispersed in water, were analyzed. Small-angle X-ray scattering was applied to thoroughly characterize nanoparticle structuring. We proved that the magnetic hyperthermia performances of nanoclusters and single nanoparticles are distinctive. Nanoclustering acts to reduce the specific heating efficiency whereas a peak against concentration appears for the well-dispersed component. Our experiments show that the heating efficiency of a magnetic colloid can increase or decrease when dipolar interactions increase and that the colloid concentration, i.e., dipolar interaction, can be used to improve magnetic hyperthermia. We have proven that the power dissipated by an ensemble of dispersed magnetic nanoparticles becomes a nonextensive property as a direct consequence of the long-range nature of dipolar interactions. This knowledge is a key point in selecting the correct dose that has to be injected to achieve the desired outcome in intracellular magnetic hyperthermia therapy.

INTRODUCTION

Magnetic hyperthermia (MH) treatment using magnetic nanoparticles (MNPs) is a promising cancer therapy, currently in clinical trials.[1,2] The mechanisms involved in MNPs heat dissipation under an alternating magnetic field are well understood for homogeneous colloids in which MNPs are widely separated so that the dipolar interaction between them is negligible.[3,4]

However, magnetic suspensions often used for biomedical applications are bidisperse systems, i.e., single nanoparticles coexisting with nanoclusters, instead of being composed of nanoparticles of nearly the same size. The particles inside the clusters are almost in contact, so they are highly interactive. Aggregation may occur in the suspension depending on the competition between attractive interactions (dipolar and van der Waals) and repulsive interactions (electrostatic and steric)[5,6] or during the chemical process of ligand exchange frequently carried out in hydrophobic nanoparticles to achieve hydrophilic character.[7] Furthermore, in biological applications, the interactions of MNPs with cells induce aggregation. During the endocytosis process, a large number of particles are enclosed in vesicles of 1 to 2 μm size.[8−10] The particles

Received: September 25, 2015
Revised: January 8, 2016
Published: January 11, 2016

DOI: 10.1021/acs.langmuir.5b03559
Langmuir 2016, 32, 1201−1213

enclosed in cellular endosomes are highly concentrated, and the magnetic interactions among them become very strong. For this reason, an understanding of the effects of aggregation and dipolar interaction on MH is crucial.

Heat dissipation under a radio-frequency (RF) field of an ensemble of homogeneously dispersed nanoparticles has been widely studied from theoretical[11−13] and experimental[14−16] points of view. However, how MNPs belonging to a nanocluster behave magnetically in a highly interactive environment and how this behavior influences their heating efficiency are still open questions.

Magnetocalorimetric[17] and electromagnetic[18] experiments have been carried out to address the influence of dipolar interactions on colloid response under RF fields, but there is not full agreement on this influence. Increases and decreases in MNP performance with increasing dipolar interaction strength have been reported.[19−24] Other authors have reported a peak in MNP performance against colloid concentration.[25,26]

For an ensemble of single-domain MNPs, the specific absorption rate (SAR) is a parameter commonly used as a figure of merit to characterize the goodness of a given combination of colloidal suspension and field characteristics to transduce the field energy into heat. An analytical expression of the SAR parameter[11]for a polydisperse ensemble of MNPs characterized by a volumetric size distribution $g_V(D)$ is given within the linear response regimen by

$$\mathrm{SAR} = \frac{\mu_o \omega H_o^{\,2}}{2\rho} \int_0^\infty \chi''(D) g_V(D)\, \mathrm{d}D \tag{1}$$

where

$$\chi''(D) = \frac{\mu_o M_s^{\,2} V}{3k_B T} \frac{\omega\tau(D)}{1 + (\omega\tau(D))^2}$$

is the out-of-phase component of the magnetic susceptibility; f ($\omega = 2\pi f$) and H_o are the field frequency and amplitude, respectively; M_s, V, ρ, and τ are the MNP specific saturation magnetization, magnetic volume, density, and relaxation time, respectively; and μ_o is the permeability of free space. The relaxation time characterizes the dynamics of the MNP coherent magnetization reversal that is governed by Néel and Brown relaxation mechanisms. For noninteracting particles of uniaxial anisotropy when the MNP magnetic moment jumps to the opposite direction without particle rotation, the time spent by the magnetic moment in a specific projection before jumping is the Néel relaxation time $\tau_N = \tau_o e^{KV/k_B T}$, where τ_o is usually 10^{-10}−10^{-9} s and K is the magnetic anisotropy energy density. When the magnetic moment orientates by particle rotation, the Brown relaxation time is given by $\tau_B = 3\eta V_H/k_B T$, where η is the medium viscosity and V_H is the nanoparticle hydrodynamic volume. Within the assumption of independence between Brown and Néel phenomena, relaxation times add in parallel and the effective relaxation time is $\tau = (\tau_N^{-1} + \tau_B^{-1})^{-1}$. When $\tau_N \ll \tau_B$ or $\tau_N \gg \tau_B$, the effective time is the smaller one.

The effects of interparticle interaction in colloidal suspensions are usually taken into account by a relaxation time modification. For weak interacting MNPs, an increase in Néel relaxation time was first proposed by Dormann et al.[27] within mean-field theory. More recently, Landi,[28,29] using a random dipolar-field approximation, also proposed an increase in the Néel relaxation time for an ensemble of monodisperse MNPs, with this being a case where the mean first-order fluctuating dipolar field contribution averages to zero. The author showed that changes in the interparticle distances might have substantial effects on the magnetization dynamics, with these effects being capable of increasing or decreasing the amount of heat released under RF; i.e., this model has theoretically predicted a peak in SAR depending on the dipolar interaction strength, unifying the different behaviors that were experimentally observed. These observations were recently supported by kinetic Monte Carlo simulations[30] of the magnetic dynamic hysteresis loop area of magnetite particles against volume concentration. The simulation displays a peak in SAR against concentration that was explained as being due to a change in the dipolar field character from demagnetizing to magnetizing.

Here, we analyze the influence of aggregation and magnetic dipolar interaction on SAR using two kinds of colloids composed of MNPs synthesized by thermal decomposition. The nanoparticles have mean sizes in the range from 10 to 18 nm and a very low size dispersion. The colloids consist of Fe_3O_4 nanoparticles coated with oleic acid (OA) and dispersed in hexane in the first case and coated with meso-2,3-dimercaptosuccinic acid (DMSA) and dispersed in water in the second case. The colloidal suspensions and their dilutions, as 1:2, 1:10, 1:50, and 1:100, were structurally characterized using small-angle X-ray scattering (SAXS). This technique allows us to carry out data acquisition under the same ambient conditions of SAR experiments and to sense various length scales, i.e., particles and clusters can be simultaneously observed. The diluted colloids are used to determine the stability of the aggregates. The colloids were magnetically characterized with dc magnetometry, and their SAR properties were determined in a wide range of field amplitudes from 16 to 52 kA/m at 145 and 260 kHz. Magnetization loops were measured at several temperatures to determine the saturation magnetization and coercive fields. From the dependence of the coercive field with temperature, the effective anisotropy constant and blocking temperature were derived. Zero-field-cooled (ZFC) and field-cooled (FC) protocols were used to establish the presence of magnetic interactions, and isothermal remanent magnetization (IRM) and dc demagnetization (DCD) protocols were used to analyze the nature of these interactions. The analysis proved that in our colloids, the magnetic interactions between MNPs have dipolar demagnetizing character and are too strong to be neglected in SAR data analysis.

Once nanoparticle structuring in the colloidal state was fully characterized, establishing the presence of nanoclusters and their sizes, shapes, and fractions, the dependence of SAR on these parameters was analyzed. SAR data were semiempirically modeled, with the input of structural and magnetic data measured with SAXS, transmission electron microscopy (TEM), and dc magnetometry, with the analytical expression given by eq 1 and taking into account dipolar interactions through a modification of the single-particle relaxation time. Finally, we chose the suspensions displaying the larger SAR and lower aggregation to carry out SAR measurements against colloid concentration. The analysis of the experimental SAR concentration dependence combined with structural and magnetic characterizations provided an experimental confirmation of the SAR behavior proposed by a random dipolar-field approximation model.[29]

New information about the heat dissipation of bidisperse suspensions is presented. We point out that the knowledge of

DOI: 10.1021/acs.langmuir.5b03559
Langmuir 2016, 32, 1201−1213

the effect of MNP aggregation on SAR may be used to select excitation field parameters to improve intracellular MH therapy.

MATERIALS AND METHODS

Synthesis of Magnetic Colloids. Monodisperse MNPs were synthesized by the thermal decomposition of the iron oleate complex ($Fe(oleate)_3$) in 1-octadecene (boiling point 315 °C) using oleic acid and oleylamine as stabilizers. The synthesized oleic acid-coated magnetite particles were finally dispersed in hexane.[33]

Briefly, precursor $Fe(oleate)_3$ was first prepared by dissolving 10.8 g of $FeCl_3 \cdot 6H_2O$ and 45 g of sodium oleate in a mixture of water (60 mL), ethanol (80 mL), and hexane (140 mL). The mixture was heated to reflux at 70 °C for 4 h with vigorous magnetic stirring. Then the system was allowed to cool to room temperature. The aqueous phase was separated from the organic phase by washing three times with a water−ethanol mixture. The organic phase was placed in a rotavapor at 60 °C for 1 h and then in an oven at 50 °C for 3 days to evaporate the organic solvent and to obtain a reddish-brown oily product. For the synthesis of oleic acid-coated MNPs, 4.5 g of the prepared $Fe(oleate)_3$ was mixed with 0.71 g of oleic acid in 50 mL of 1-octadecene in a round-bottomed flask.[33] The mixture was stirred (100 rpm) and slowly heated with a heating mantle (2 °C/min 1 for T < 100 °C and 3 °C/min for T > 100 °C) until reflux (315 °C) and left at this temperature for 1 or 2 h depending on the desired final particle size. In the first case, MNPs of 10 and 11 nm were obtained, and in the second case, the MNP sizes were larger (17 and 18 nm). The resulting black mixture was washed several times with ethanol, and the particles were separated using a magnet. The resulting black solid was redispersed in hexane for long-term storage.

Oleic acid-coated MNPs were transferred to water by a ligand-exchange technique, substituting the oleic acid with a hydrophilic molecule, meso-2,3-dimercaptosuccinic acid (DMSA). In a typical experiment, 50 mg of oleic acid-coated MNPs suspended in hexane was washed a few times with ethanol, precipitated by a magnet, and resuspended in 20 mL of toluene. This suspension was added to DMSA dissolution in dimethylsulfoxide (DMSO) (90 mg of DMSA in 5 mL of DMSO) and gently stirred for 72 h. After this, the MNPs attached to the glass reaction bottle were resuspended in ethanol, sonicated, and then centrifuged at 9000 rpm for 20 min. This process was repeated four or five times. After that, the MNPs were resuspended in water and the pH was increased to 10 to improve the MNP stability by electrostatic repulsions of COO^- and thiol groups. The thiol groups that do not form disulfide bonds are deprotonated at this pH. This suspension was dialyzed for 3 days in a 12−14 kDa membrane to eliminate the excess DMSA.

The aqueous colloids concentration $[x]$ was determined by inductively coupled plasma-optical emission spectrometry (ICP-OES, PerkinElmer Optima 2100 DV ICP). For organic colloids, the mass concentration was determined from saturation magnetization values assumed to be equal to those measured in the corresponding aqueous colloids.

Structural Characterization. The MNP morphology and size distribution were determined by TEM microscopy on OA-coated nanoparticles using a TEM JEOL 2000FXII with an accelerator potential of 200 kV that allows a resolution of 0.14 nm. Samples were prepared by drying 1 drop of a diluted suspension on a carbon-coated copper grid.

The hydrodynamic size (D_H) was measured by dynamic light scattering (DLS) from a dilute suspension of nanoparticles in water at pH 7 in a standard cuvette using a Zetasizer NanoZS device (Malvern Instruments).

SAXS measurements were conducted at room temperature at the D01B-SAXS beamline of the National Synchrotron Radiation Laboratory (LNLS, Campinas, Brazil) using an X-ray wavelength of λ = 1.822 Å and sample-to-detector distances of 610 and 1976 mm. This allowed us to determine the scattering intensity $I(q)$, with q being the modulus of the scattering vector, over a q range extending from 0.07 to 5.55 nm^{-1}. Prior to SAXS measurements, the liquid colloidal solutions were sonicated and then injected into a 1-mm-thick sample holder for liquids between two parallel 25-μm-thick ruby mica disks. Another set of SAXS measurements under different dilution conditions were carried out using a NanoStar SAXS camera equipped with a Xenox X-ray source with a wavelength of λ = 1.541 Å and a sample-to-detector distance equal to 1070 mm, covering a q range from 0.08 to 3.50 nm^{-1}. For SAXS measurements, the as-prepared colloids were diluted, sonicated, and immediately injected into a 2-mm-thick quartz capillary sample holder. An alloy of glassy carbon and aluminum was used as a standard (T_{CvAl} = 0.009294) to determine the sample transmittance.

A correction for background and solvent scattering was achieved by subtracting from the data, previously corrected by absorption, the scattering registered from a sample holder filled with solvent. Water was used as a secondary standard to express data as a differential cross section $d\Sigma/d\Omega$ and to combine data acquired with two different camera lengths.

Magnetic Characterization. Magnetic measurements were performed on liquid or frozen colloids depending on the measurement temperature. A 50 μL colloidal suspension were sealed in a heat-shrinkable tube to prevent sample evaporation and spills. Specific magnetization (M) was obtained against the applied magnetic field H at different temperatures using a superconducting quantum interference device (SQUID) magnetometer with a maximum field of $\mu_o H_{max}$ = 2.5 T. Data were plotted after subtracting the diamagnetic contribution due to the solvent and sample holder. Zero-field-cooled (ZFC) and field-cooled (FC) protocols were carried out under a dc field of 8 kA/m at 5 K/min. To avoid the jump in magnetization close to the solvent melting point,[21,31] measurements were performed from 5 to 170 K and from 5 to 250 K for hexane and water-based colloids, respectively.

The isothermal remanent magnetization (IRM) and dc demagnetization (DCD) were measured at 5 K.[32] To carry out the IRM measurement, the sample is cooled at zero field and then a field H is applied for a short time; after the field is removed, the remanent magnetization is measured. This procedure was repeated with increasing H values until a saturation field of 4000 kA/m was reached. DCD measurements begin in the fully magnetized state at 5 K. The sample is subjected to a saturation field of 4000 kA/m. Then a negative field H is applied for a short time and turned off, and the magnetization is measured. The process was iterated by varying the negative field from −4 to −4000 kA/m.

Magnetocalorimetric Determination of SAR. Time-dependent calorimetric experiments for determining SAR were conducted by exposing 1 mL of the aqueous suspensions, held in a clear glass dewar, to alternating magnetic fields of 145 and 260 kHz and several field amplitudes in the range from 16 to 52 kA/m. The field generator, a Hüttinger (2.5/300), consists of a resonant RLC circuit holding a water-refrigerated five-turn coil of 5 cm inner diameter. An optical fiber sensor connected to a calibrated signal conditioner (Neoptix) with an accuracy of 0.1 °C was used. During the experiment, the sensor was held in the center of the sample. The colloid temperature was kept below 50 °C in order to minimize solvent evaporation and prevent its destabilization. Measurements were made in triplicate.

Experimental SAR was determined from the initial slope dT/dt of the heating curve as

$$SAR_e = \frac{c}{[x]}\frac{dT}{dt} \tag{2}$$

where c is the volumetric heat capacity of the liquid carrier.

RESULTS AND DISCUSSION

To analyze the influence of aggregation and magnetic dipolar interaction on SAR, we have chosen to work with colloidal suspensions of Fe_3O_4 nanoparticles displaying very low size dispersity, high uniformity in shape, and saturation magnetization as close as possible to the bulk value. To this end, magnetite nanoparticles of 10, 11, 17, and 18 nm were synthesized by the thermal decomposition of an iron

DOI: 10.1021/acs.langmuir.5b03559
Langmuir 2016, 32, 1201−1213

Table 1. Colloid Structural Parameters[a]

colloid	$[x]$ ($mg_{Fe_3O_4}$/mL)	D_{TEM}(nm)	sd_{TEM} (nm)	D_{saxs} (nm)	σ	sd_{saxs} (nm)	d_f	ξ (nm)	α	$\Delta\eta_e(10^{11}$ cm$^{-2})$	D_H (nm)	n_ξ^p
O10	4.57	10.07	0.92	11.46	0.06	0.72	2.96	54.70	0.199	2.9	50	46
O11		10.78	0.94	14.02	0.01	0.07	2.99	78.45	0.152		45	85
O17		16.60	2.18	17.24	0.17	2.94	2.45	60.20	0.060		60	23
O18	4.81	17.77	3.66	16.90	0.17	3.03				2.3	60	0
DMSA10	14.83			10.98	0.08	0.92	2.90	57.70	0.280	2.1	80	88
DMSA11	6.92			13.44	0.07	0.93	2.85	29.92	0.600	2.5	65	7
DMSA17	2.88			16.88	0.17	2.99	2.77	53.85	0.319	0.4	80	23
DMSA18	6.50			16.02	0.21	3.57	2.93	43.20	0.130	2.2	80	14

[a] $[x]$ is the colloid concentration and D_{TEM} and sd_{TEM} are the mean particle size and standard deviation calculated from Gaussian fits of TEM histograms, respectively. $D_{saxs} = 2R_oR_oe^{\sigma^2/2}$ is the mean particle diameter, and $sd_{saxs} = D_{saxs}(e^{\sigma^2} - 1)^{1/2}$ is the standard deviation calculated from SAXS fitted data using the number LogNorm radii distribution, with σ being the standard deviation of the $\ln(R/R_0)$ variable and R_0 being the median particle radius. ξ and d_f are the size and fractal dimension of the nanoclusters, and α is the fraction of nanoclustered MNPs. $\Delta\eta_e$ is the scattering-length difference per unit volume between magnetite and the dispersing liquid phase. D_H is the hydrodynamic diameter, and n_ξ^p is the mean particle number per nanocluster (quotient between nanocluster volume and particle volume).

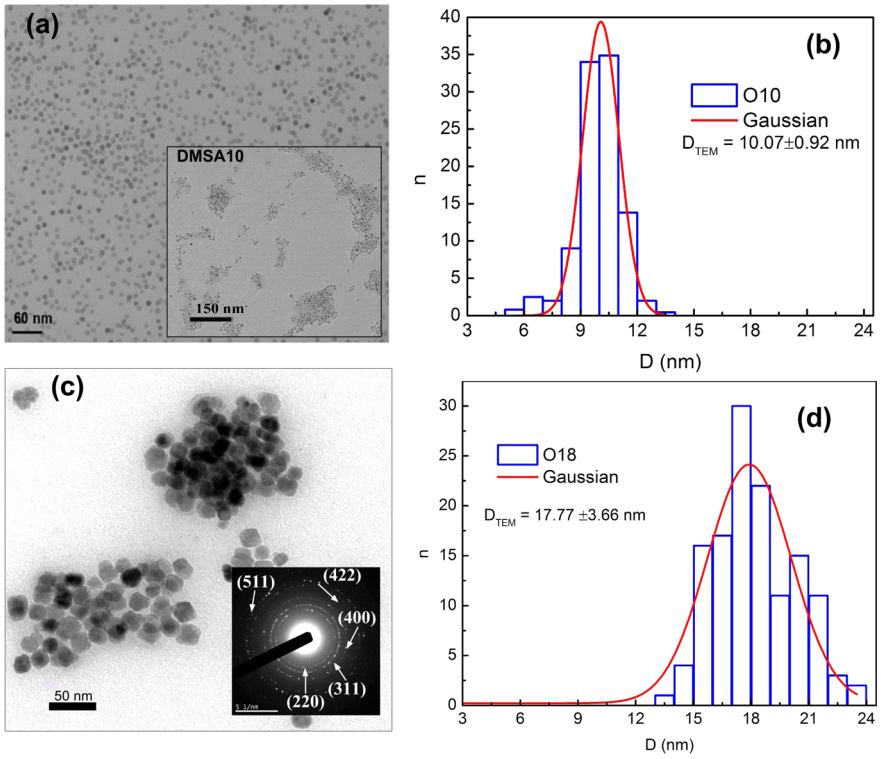

Figure 1. TEM images and size histograms. (a, b) O10 sample. Inset: TEM image of the DMSA10 sample. (c, d) O18 sample. Inset: electron diffraction pattern.

coordination complex, $Fe(oleate)_3$ in 1-octadecene.[33] In this way, hydrophobic particles of magnetite coated with oleic acid were obtained and resuspended in hexane. These colloids were labeled as O10, O11, O17, and O18. These suspensions are not suitable for biomedical applications, but their study helps us to understand the structuring and magnetic behavior of the hydrophilic particles that were later derived from them by ligand exchange.[7] The surfaces of the oleic acid-coated MNPs were modified with meso-2,3-dimercaptosuccinic acid (DMSA) to achieve hydrophilicity for water transfer. These colloids were labeled as DMSA10, DMSA11, DMSA17, and DMSA18. Colloid concentrations are listed in Table 1.

Bidisperse Structure of Magnetic Colloids. TEM microscopy, carried out on samples of dried colloids, was used to determine the MNP morphology and size distribution. Representative TEM images of O10, O18, and DMSA10 dried samples are shown in Figure 1. (For a TEM image of O11 MNPs, see Figure 1 in Supporting Information.) The MNPs show spheroidlike shape and size uniformity. Histograms obtained by counting over 100 particles were well fitted using Gaussian distributions (Figure 1b,d). Fitted mean size value D_{TEM} and standard deviation sd_{TEM} are listed in Table 1. The inset in Figure 1c displays one of the electron diffraction patterns. This pattern indicates good crystallinity and was indexed by assuming a cubic spinel structure (space group $Fd3m$ of magnetite and maghemite phases). The synthesis process used in this work was earlier optimized to obtain magnetite nanoparticles, to avoid the formation of core/shell structures, and to yield highly crystalline particles.[34,47] However, we cannot discard some oxidation of magnetite nanoparticles to maghemite, with this effect taking place mainly at the nanoparticle surface and being particularly important for

DOI: 10.1021/acs.langmuir.5b03559
Langmuir 2016, 32, 1201−1213

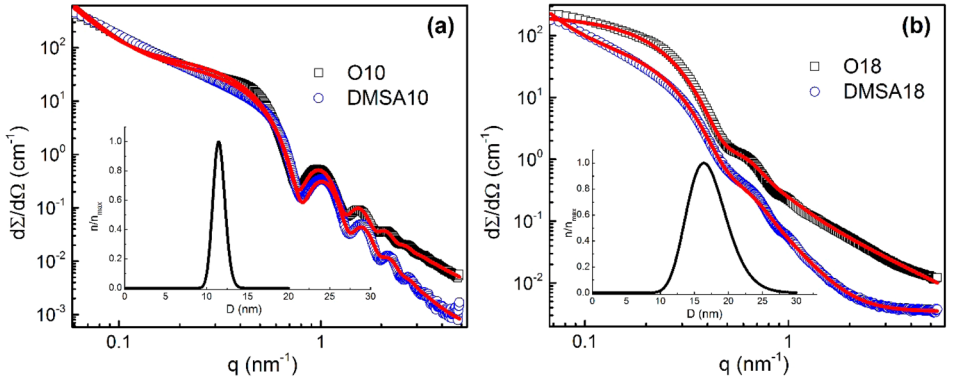

Figure 2. log−log representation of colloid scattering curves expressed as the differential cross section ($d\Sigma/d\Omega$) vs scattering vector modulus q of (a) O10 and DMSA10 colloids and (b) O18 and DMSA18 colloids. Solids lines are the modeled functions (eq 3) that best fit the experimental SAXS curves. Inset: Fitted log-normal size distributions.

very small particles (smaller than 5 nm).[35] Mossbauer spectroscopy analysis has shown that particles larger than 10 nm preserve the magnetite core for years.[36] Besides, the magnetic properties of both phases are quite similar, including saturation magnetization. Therefore, if some degree of oxidation has occurred, then no noticeable effect on dipolar interactions is to be expected.

SAXS was applied to determine the structuring features of colloidal suspensions of magnetite nanoparticles under the same ambient conditions of the SAR experiment. In Figure 2, a double-logarithmic plot of the scattering curves of aqueous and hexane colloids is shown. The scattering intensity, expressed as the differential cross section, displays power law behavior for the low-q range ($q < 0.4$ nm^{-1}) instead of the typical Guinier behavior of a single particle, revealing the presence of nanoclusters, and oscillatory behavior (fringes in the 2D SAXS pattern) damped with the Porod law for the 0.4 nm$^{-1} \leq q \leq 2$ nm^{-1} characteristic of single particles. The oscillations are somehow smooth due to the finite size distribution.

These oscillations are characteristic of spherical nanoparticles with narrow radii dispersions. For a narrower particle size distribution, sharper fringes are expected. The oscillations are better defined in O10, DMSA10, O11, and DMSA11 (Figure 2a and Figure 2a in the SI, respectively) than in O17, DMSA17 and O18, DMSA18 SAXS curves (Figure 2b in the SI and Figure 2b, respectively). This qualitatively indicates that smaller MNPs display narrower size dispersions than larger MNPs.

A knowledge of the first-minimum positions q_{1mn} of the SAXS curves plotted in Figure 2a and Figure 2a of the SI allowed us to obtain preliminary estimates of the average sphere radius as $R = 4.50/q_{1min}$, which results in $\langle R\rangle \approx 5.7$ nm for O10 and DMSA10 samples and $\langle R\rangle \approx 7.0$ nm for O11 and DMSA11 samples. For q values larger than 2 nm^{-1}, the Porod law behavior is somehow masked by a q-independent incoherent background.

To retrieve structural information from both nanoclusters and single particles, SAXS data were fitted using a spherical form factor, in agreement with TEM observations, and a log-normal size distribution. This distribution was chosen instead of the Gaussian one to avoid ad hoc symmetry impositions.

Aggregation was taken into account using an analytical form for the structure function $S(q\xi, R_o)$ derived within a fractal model of aggregation in which the power law form of the scattering function is limited by a finite cluster size ξ, introduced in the pair correlation function as an exponential cutoff $h(R, \xi) = \exp[-R/\xi]$[37,38] and by the particle finite size (radius R_o) as

$$S(q\xi, R_o) = 1 + \frac{d_f\Gamma(d_f - 1)}{(qR_o)^{d_f}} \frac{\text{sen}[(d_f - 1)\tan^{-1}(q\xi))]}{(1 + 1/(q\xi)^2)^{d_f - 1/2}}$$

where d_f is the fractal dimension of the nanoclusters and Γ is the gamma function.

Scattering arising from a bidisperse system composed of a fraction α of particles inside nanoclusters coexisting with a fraction $1 - \alpha$ of non-nanoclustered single particles is considered by expressing SAXS curves as

$$\frac{d\Sigma(q)}{d\Omega} = [1 - \alpha + \alpha S(q\xi, R_o)]\frac{d\Sigma_{sp}(q)}{d\Omega} \quad (3)$$

where the scattering of diluted polydisperse spherical particles $\frac{d\Sigma_{sp}(q)}{d\Omega}$ is given by

$$\frac{d\Sigma_{sp}(q)}{d\Omega} = N_s(\Delta\eta_e)^2 \int_0^\infty V^2 \left[3\frac{\text{sen}(qR) - qR\cos(qR)}{(qR)^3}\right]^2 f(R)\, dR$$

with N_s being the particle number density, $\Delta\eta_e$ being the scattering-length difference per unit volume between particles and the liquid phase, and $f(R)$ being the log-normal number distribution of particles characterized by the median radius R_o ($D_{saxs} = 2R_o e^{\sigma^2/2}$) and by the standard deviation σ of the variable $\ln(R)$. The theoretically calculated $\Delta\eta_e$ values are 3.23 $\times 10^{11}$ and 3.52 $\times 10^{11}$ cm^{-2} for Fe_3O_4 MNPs dispersed in water and hexane, respectively. The SAXS curves were well fitted by modeled functions defined by eq 3, which take into account the contributions of both isolated nanoparticles and nanoclusters.

The SAXS intensity functions defined by eq 3 that best fit the experimental SAXS curves are plotted as solid lines in Figure 2 and Figure 2 of the SI, and the fitted size distribution is plotted as the inset in Figure 2. Relevant associated parameters are listed in Table 1. The mean particle sizes D_{SAXS} are in good agreement with the average D_{TEM} values, and cluster sizes ξ are the same order of magnitude as D_H values derived from DLS measurements. The hydrodynamic size of the nanoparticles, i.e., the diameter of a diffusing particles in suspension, is always larger than the nanoparticle core diameter, even when particles are isolated. DLS measurements include the coating on the nanoparticle surface and the hydration layer. The reported DLS

DOI: 10.1021/acs.langmuir.5b03559
Langmuir 2016, 32, 1201−1213

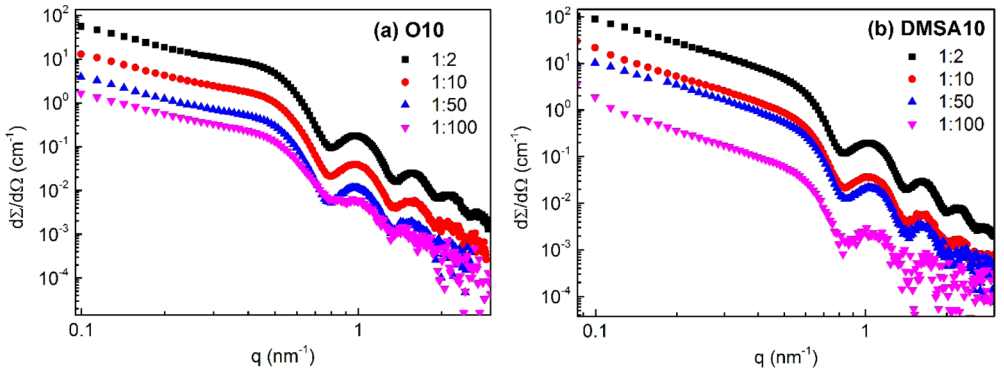

Figure 3. log−log representation of colloid scattering curves expressed as the differential cross section ($d\Sigma/d\Omega$) vs scattering vector modulus q obtained at various dilutions. (a) O10 colloid and (b) DMSA10 colloid.

mean values are weighted averages that are generally dominated by nanoclusters and/or large particles.

We have determined nonvanishing number fractions ($\alpha > 0$) for all SAXS curves with the exception of the O18 colloid. Nonvanishing α values indicate the coexistence of isolated particles with nanoclusters (eq 3). The value $\alpha = 0$ for sample O18 implies that the nanoparticles in this particular case are well dispersed in the liquid; i.e., the entire curve was well fitted with $S(q\xi, R_o) = 1$. In spite of being composed of the same magnetite core as O18 where no aggregation occurs, the aggregation observed for sample DMSA18 indicates that the surface modification employed favors MNP aggregation. This kind of aggregation was previously inferred for the present type of colloidal suspension and was explained on the basis of chemical arguments by Roca et al.[15]

Fractal dimensions derived from fitting procedure are between 2.45 and 3.00, indicating that MNPs are nanoclustered in partially compacted three-dimensional structures. Less-compacted chainlike structures would have been characterized by $1 < d_f < 2$. For all of the samples, the fraction of nanoclustered MNPs is larger for DMSA-coated nanoparticles than for OA-coated nanoparticles, supporting the idea that the surface-modification process induces aggregation.

To evaluate the stability of the nanoclusters, samples O10, O17, DMSA10, and DMSA17 were selected to perform SAXS measurements at different colloid concentrations. Aliquots of the as-prepared colloids of concentration $[x]$, listed in Table 1, were sonicated for 15 min before and after dilution to 1:2, 1:10, 1:50, and 1:100 and immediately injected into the sample holder and measured. Scattering curves of O10 and DMSA10 diluted samples are shown in Figure 3. Similar results for the other samples are shown in Figure 3 of the SI. It is observed that the shape of the scattering curves remains unchanged after sonication and dilution, indicating that the aggregation is stable. The values of $d\Sigma/d\Omega$ extrapolated to $q = 0$ decrease with dilution, evidencing its dependence on $N_\xi \Delta\eta_e^2$, with N_ξ being the number of nanoclusters in the sample. The mean number of particles, n_ξ^p, in the nanoclusters, listed in Table 1, was calculated as the ratio between the nanocluster volume V_ξ and particle volume including the coating, as 1.91 and 1.00 nm for the OA and DMSA molecules, respectively.

In summary, our SAXS analysis demonstrated that all studied colloids, with the exception of O18, are bidisperse, i.e., composed of nanoclusters coexisting with individual particles, and this aggregation is stable and independent of concentration (within the limits of our measurements). The surface modification of OA-coated nanoparticles for the water-transfer procedure favors aggregation.

Magnetic Behavior. To analyze SAR, besides structural characterization, complete magnetic characterization is also needed. Then, magnetic nanoparticle properties, such as the mean magnetic moment $\langle\mu\rangle$, saturation magnetization M_s, effective magnetic anisotropy energy density K_{eff}, and blocking temperatures were measured and used to simulate SAR behavior using eq 1 for comparison with experimental results.

To this end, specific magnetization M vs applied field H curves were measured at several temperatures between 5 and 300 K. Figure 4 shows the magnetic loops measured at 300 K for samples DMSA10 and DMSA18. These curves display typical superparamagnetic behavior.

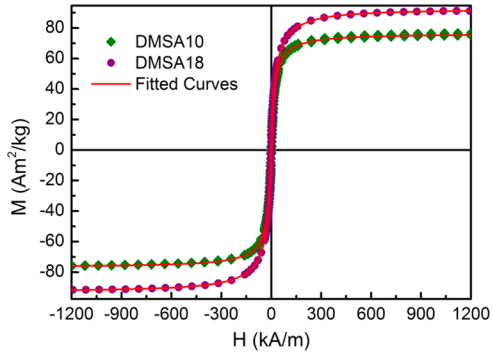

Figure 4. Specific magnetization M vs applied magnetic field H measured at 300 K for samples DMSA10 and DMSA18. Continuous red lines represent the best fits obtained using eq 4.

The magnetic loop of this ensembles of nearly monodisperse particles can be described by $M = M_s L(x)$, where $L(x)$ is the Langevin function and $x = \mu_0\mu H/k_B T$, with μ being the particle magnetic moment and $M_s = N_p\mu$ being the saturation magnetization corresponding to N_p particles per mass unit. To describe the particle size distribution, a log-normal distribution of magnetic moments $g(\mu)$ with median μ_m and standard deviation σ_μ was chosen, instead of the Gaussian distribution, to avoid ad hoc symmetry impositions, in the same way that we have proceeded for SAXS data analysis. Experimental data was fitted with

$$M(H) = N_p \int_0^\infty \mu \left[\coth\left(\frac{\mu\mu_o H}{k_B T}\right) - \frac{k_B T}{\mu\mu_o H} \right] g(\mu)\, d\mu + \chi_p H \quad (4)$$

DOI: 10.1021/acs.langmuir.5b03559
Langmuir 2016, 32, 1201−1213

Table 2. Magnetic Properties[a]

colloid	$\langle\mu\rangle$ (μ_B)	M_s ($Am^2/kg_{Fe_3O_4}$)	K_{eff} (kJ/m^3)	T_i (K)	$\langle T_B^H\rangle$ (K)	H_{int} (kA/m)	SAR_e (W/g)	ILP (10^{-12}J m^2/g A^2)	SAR_R (W/g)	K_{RF} (kJ/m^3)
O10	25836		22.11	153	60.48		70.9[c]	0.100	16.38	32.27
DMSA10	21159	76.71	19.18	202	58.64	−11.93	22.6[c]	0.032	30.04	17.60
DMSA11	19477	78.71	19.10	204	86.30	−11.37	21.0[d]	0.114	163.41	12.89
O18	32209		21.50	256[b]	161.40		383.9[d]	2.089	2943.4	
DMSA18	31772	75.99	17.00	256[b]	155.90	−17.80	67.7[d]	0.368	2101.7	6.14

[a]$\langle\mu\rangle$ is the mean magnetic moment, and M_s is the saturation magnetization at 300 K. K_{eff} and $\langle T_B^H\rangle$ are the anisotropy constant and the mean blocking temperature determined from H_c vs T analysis, respectively. T_i is the irreversibility temperature determined from the ZFC−FC curves, and SAR_e and SAR_R are the specific absorption rates determined from magnetocalorimetric measurements and calculated with eq 1, respectively. K_{RF} is the anisotropy constant derived from SAR_e values. [b]T_i values derived from H_c vs T analysis. [c]SAR measured at 260 kHz and 52.0 kA/m. [d]SAR measured at 145 kHz and 35.6 kA/m.

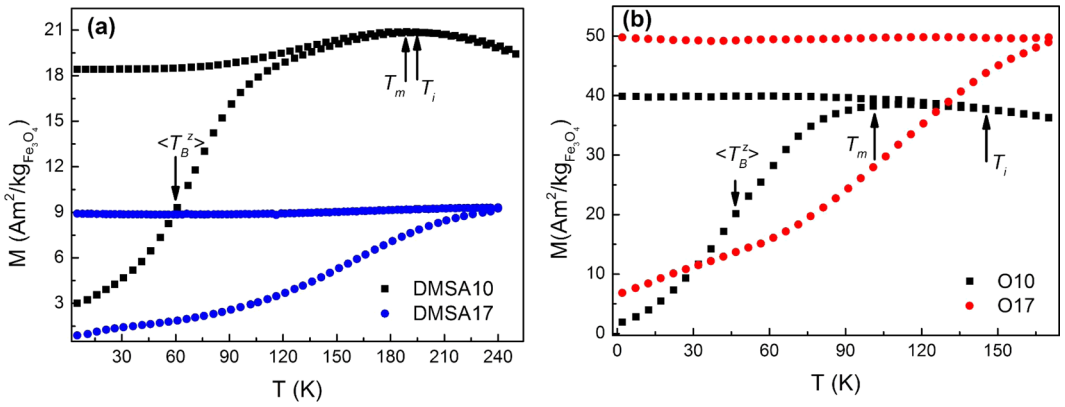

Figure 5. ZFC and FC curves measured at 8 kA/m and 5 K/min for samples (a) DMSA10 and DMSA17 and (b) O10 and O17. The black arrows indicate blocking $\langle T_B^z\rangle$, maximum T_m, and irreversibility T_i temperatures in the curves of DMSA10 and O10 frozen colloids.

where χ_p is the high field susceptibility. The last term of eq 4 combines negative contributions due to the diamagnetic response of the liquid with positive contribution due to a magnetically frustrated layer around the MNP. The parameters that resulted from the best fits using eq 4 are listed in Table 2, and fitted curves are shown in Figure 4. M_s values of DMSA-coated magnetite nanoparticles are within the reported range (70−80 A m^2/kg).[33]

Strong dipolar interactions are visualized in M vs T curves obtained under ZFC−FC protocols shown in Figure 5 for DMSA10, DMSA17, O10, and O17 samples. At low field values, the magnetic anisotropy energy and the dipolar interaction among particles determine the magnetization temperature dependence observed in FC and ZFC curves. The ZFC curves of O10 and DMSA10 exhibit a maximum at temperature T_m, and ZFC bifurcates from the FC curve at the irreversibility temperature T_i. At temperatures higher than T_i, all of the MNPs are unblocked. The absence of T_i in the ZFC−FC curves of O17 and DMSA17 samples indicates that not all of the MNPs become unblocked in the temperature range of our measures. This fact reveals that aggregation and strong dipolar interaction between particles results in higher blocking temperatures. As the temperature decreases from T_i, the FC magnetization displays only a slight variation. The constancy of M over almost the whole FC curve is also a signature of a highly interacting system.[39] The formation of glasslike peaks and magnetic anomalies in ZFC−FC data has been reported for Fe_3O_4 nanoparticles, mean size ∼14 nm, suspended in hexane and dodecane at a concentration of 20 mg/mL, with these features related to the liquid carrier melting transition and the particle blocking influenced by dipolar interactions.[31] No cusp was observed for our suspension in either hexane or water. We have observed a sharp magnetization jump as reported in ref 21 for 13 nm γ-Fe_2O_3 nanoparticles dispersed in hexane because of coupling with the solvent melting transition. When this occurs, the MNPs can rotate and align their anisotropy axes easily in the direction of the field. As a consequence, ZFC would correspond to a system with random anisotropy orientations; meanwhile, FC would correspond to a system with some degree of order. If the melting temperature of the solvent is crossed in the upward direction, then magnetization jumps within a region close to this temperature (177 and 273.15 K for hexane and water, respectively), owing to easy axis rotation. Because the aim of our ZFC and FC measurements was just to prove that the dipolar interaction among the MNPs is not neglectable and to determine the anisotropy constant, our ZFC−FC measurements were performed at temperatures below the liquid carrier melting points. The irreversibility temperatures T_i are reported in Table 2.

To determine the anisotropy energy density, the behavior of H_c against temperature was analyzed. At T = 0 K, the Stoner−Wohlfarth model predicts for an arrangement of noninteracting MNPs a coercive field equal to the anisotropy field $H_K = 2K_{eff}/M_s$. For the thermally activated process,[40] the coercive field H_c tends to zero when the temperature increases and becomes null at the blocking temperature T_B^H. For higher temperatures, the MNPs display superparamagnetic behavior. For an assembly of randomly oriented single-domain MNPs displaying polydispersity, T_B^H is replaced by its mean value $\langle T_B^H\rangle$, and the effects of dipolar interactions are considered through an effective anisotropy energy density K_{eff} as

DOI: 10.1021/acs.langmuir.5b03559
Langmuir 2016, 32, 1201−1213

$$H_c = 0.48\frac{2K_{eff}}{\mu_o M_s}\left(1 - \left(\frac{T}{\langle T_B^H\rangle}\right)^{1/2}\right) \quad (5)$$

Examples of the temperature dependence of H_c corresponding to samples O18 and DMSA18 are shown in Figure 6. The

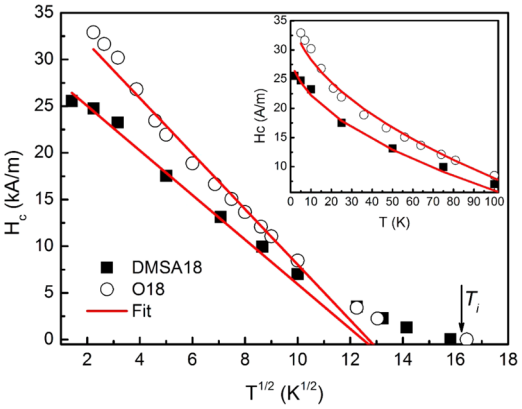

Figure 6. Plot of the coercive field H_c vs $T^{1/2}$ for O18 and DMSA18 colloids. Lines represent the best fit achieved with eq 5. Inset: Detail of the fitted range data.

temperature dependence of H_c corresponding to samples O10 and DMSA10 is shown in Figure 4 of the SI. In the H_c vs $T^{1/2}$ plot, the intercept of a linear fit is proportional to the K_{eff}/M_s ratio and the intercept at $H_c = 0$ is proportional to the mean blocking temperature $\langle T_B^H\rangle$. Deviations from linear behavior are due to the size dispersion. For this reason, the data show a null H_c value at a T_i larger than $\langle T_B^H\rangle$, with T_i being the irreversible temperature, i.e., the temperature at which the largest nanoparticles unblock.

Best fits are represented by continuous red lines in Figure 6, and fitted parameters are listed in Table 2.

The mean blocking temperatures deduced from H_c vs T data are consistent with those obtained from the ZFC−FC curves. The K_{eff} values of OA-coated MNPs are larger than for the DMSA-coated MNP. This fact may be related to the small shape anisotropy contribution.

Next, a quantitative determination of the dipolar field originating in the magnetic interaction between particles was obtained from IRM and DCD measurements carried out at 5 K. In Figure 7, the remanent magnetization, measured at null field, plotted vs magnetizing (IRM) or demagnetizing (DCD) fields is shown for the DMSA10 colloid. Similar data for DMSA11 and DMSA18 are shown in the SI.

For noninteracting MNPs, the normalized remanent magnetizations $m_{IRM} = M_{IRM}(H)/M(\infty)$ and $m_{DCD} = M_{DCD}(H)/M(\infty)$ can be described by the Wohlfarth relation:[41] $m_{DCD} = 1 - 2m_{IRM}$. Deviations from this behavior are due to interactions.

Plots of the magnitude $\delta M = m_{DCD} - (1 - 2m_{IRM})$, which quantify such deviations, are shown in Figure 7b. Typically, negative δM peaks are associated with demagnetizing magnetostatic (dipolar) interactions and positive peaks are related to exchange interactions.[42] For all of the samples, δM values smaller than zero are observed at low H values, indicating demagnetizing dipolar interactions, i.e., the ensemble of MNPs is more easily demagnetized than magnetized.[43] When the applied field overcame the dipolar field, δM tended to zero.

Alternatively, the Wohlfarth relation can be expressed in terms of irreversible susceptibilities as $\frac{dm_{DCD}}{dH} = 2\frac{dm_{IRM}}{dH}$ (insets of Figure 7). The distance between peaks is related to the mean interaction field[44,45] $H_{int} = \frac{H_{DCD} - H_{IRM}}{2}$ where H_{DCD} and H_{IRM} are the fields at which $dm_{DCD,IRM}/dH$ curves display a maximum. For all of our samples, H_{DCD} is larger than H_{IRM}, in agreement with dipolar interactions having demagnetizing character. Values of H_{int} are listed in Table 2. The largest magnetic dipolar energy appears for the DMSA18 sample.

SAR Measurements. SAR was experimentally determined by measuring the temperature increase of the colloidal suspension exposed to a radio-frequency field. Typical heating curves are shown in Figure 8a for O10 and DMSA10 colloids exposed to fields of 260 kHz and 52.0 kA/m and for O18, DMSA11, and DMSA18 colloids exposed to fields of 145 kHz and 35.6 kA/m. SAR_e values were calculated from dT/dt using eq 2, concentration $[x]$ values listed in Table 1, and liquid carrier volumetric heat capacities c of 4.184 J/mL °C for water and 1.438 J/mL °C for hexane. SAR_e values are listed in Table 2. The SAR_e field-amplitude dependence is shown in Figure 8b, which is consistent with a quadratic law (red lines in Figure 8b), as predicted by eq 1.

Using parameters determined by the structural and magnetic characterizations (D, sd, D_H, M_s, and K_{eff}), viscosity values at 300 K ($\eta = 0.7978 \times 10^{-3}$ Pa·s for water and $\eta = 2.94 \times 10^{-4}$ Pa·s for hexane[46]), and $\tau_o = 10^{-10}$ s, τ_N and τ_B were calculated for all of the colloids. It was found that $\tau_N \ll \tau_B$ for all of the samples except for O18, consistent with the occurrence of the

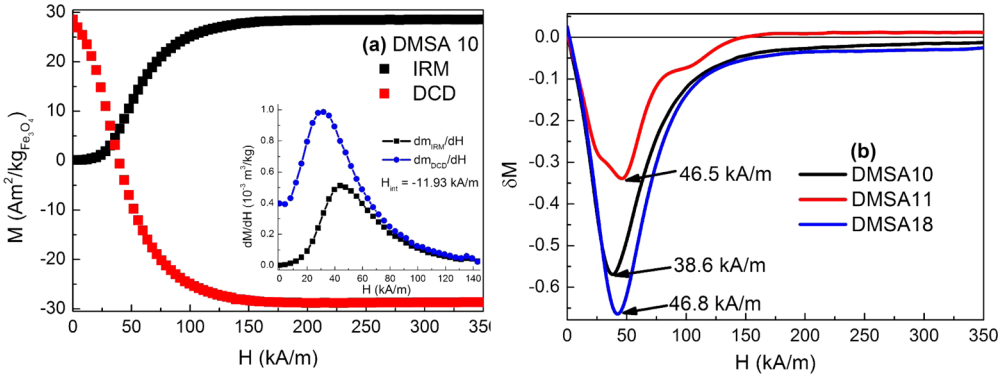

Figure 7. (a) IRM and DCD diagrams for DMSA10 colloid. Inset: irreversible susceptibility dm_{DCD}/dH and dm_{IRM}/dH curves. (b) δM plots derived as $\delta M = m_{DCD} - (1 - 2m_{IRM})$.

DOI: 10.1021/acs.langmuir.5b03559
Langmuir 2016, 32, 1201−1213

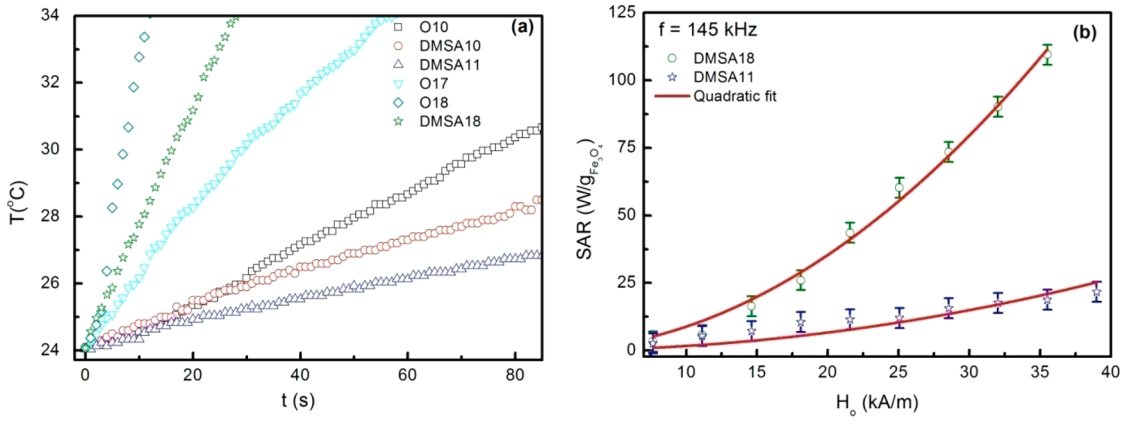

Figure 8. (a) Heating curves (T vs t) of samples O10 and DMSA10 measured at 260 kHz and 52.0 kA/m and of samples O17, O18, DMSA11, and DMSA18 measured at 145 kHz and 35.6 kA/m with the concentrations listed in Table 1. (b) SAR_e calculated from heating curves registered at 145 kHz vs field amplitude H_o. Continuous red lines represent the best quadratic fit.

Néel relaxation mechanism and in agreement with data previously reported for similar particles.[47] Calculated τ_B and τ_N values are listed in Table 1 of SI. SAR values calculated at the measuring condition (f and H_o) using eq 1, labeled as SAR_R, are listed in Table 2. The SAR_R values do not agree neither with the SAR_e values nor with the observed trend. This fact indicates that it is not enough, with respect to reproducing SAR_e results, to take into account dipolar interactions and aggregation by just a modification of the nanoparticle relaxation time using the effective anisotropy value. As was discussed above, the MNPs interact among them, with the more interactive particles composing nanoclusters. To compare measurements performed at different field frequencies and amplitudes, the intrinsic lost power, ILP = SAR/fH_0^2, parameter[14] is commonly used. The ILP values of our samples range from 0.04 to 2.89 nH m^2/kg$_{Fe}$, which are of the same order as those previously reported in the literature.[14]

Experimentally, a decrease in ILP is observed when the nanocluster size and number of particles in the nanoclusters increase (Figure 9a,b). Because the ILP parameter disregards the out-of-phase susceptibility frequency dependence, the effective anisotropy constant K_{RF} was estimated from SAR_e through eq 1. The K_{RF} values, listed in Table 2, were used to extrapolate SAR measured at a given f and H_o condition to other conditions (effective relaxation times calculated with K_{RF} are shown in Table 1 of the SI). This procedure can be applied because only structural and magnetic parameters that do not change with f and H_o are used. Both measured and extrapolated SAR values and the experimental ILP ones are plotted in Figure 9a–c against parameters determined by SAXS that characterize aggregation. These results indicate that aggregation lowers the SAR.

Data previously acquired for similar MNPs,[47] where the hydrodynamic size was used as an estimate of the degree of aggregation, showed that experimental SAR values decrease with increasing D_H, which is consistent with our present results. SAR (or ILP) values, reported in ref 47 when plotted vs the number of particles per nanocluster (estimated from the quotient of hydrodynamic and particle volume), display decreasing behavior. Nanoclustering effects on SAR have been analyzed by comparing SAR values of confined and unconfined assemblies of 10 nm Fe_3O_4 nanoparticles.[24] The confined systems consisted of nanoparticles uniformly embedded in the matrix of 100 nm polystyrene spheres, both uncoated and covered with a thin layer of silica. The unconfined ones were free nanoparticles, both uncoated and coated with poly(acrylic acid), well dispersed in water. The authors show that well-dispersed MNPs display larger SARs than nanospheres, in aggreement with our results. However, increasing SAR with increasing nanocluster size has also been reported[22] for iron oxide nanoflower-like structures. These nanoflowers are composed of several single grains that exhibit the same crystalline orientation, giving evidence of a unique magnetic organization of all of the particles in the nanocluster, i.e., the alignment of the MNPs' anisotropy axes. As observed in the inset of Figure 1c, electron diffraction patterns demonstrate that our colloids exhibit randomly distributed crystalline orientation consistent with randomly oriented anisotropy axes.

Next, because our colloids are composed of stable clusters and single MNPs, SAR measurements were carried out in diluted colloids to analyze the effect of dipolar interaction on the SAR of the single MNP component. We have selected O18 and DMSA18 colloids for this analysis (Figure 10a,b) because of their high SAR_e and low aggregation. In Figure 10a, the SAR_e of DMSA18 colloid shows a peak at around $[x]$ = 2 mg/mL, proving that SAR can be increased or reduced by dipolar interactions. This result unifies the different viewpoints on the behaviors experimentally observed by other authors, claiming an increase and decrease in SAR[19−23,31] with an increasing strength interaction. The nonmonotonic behavior of SAR with nanoparticle concentration at a frequency of 107 kHz and field amplitudes of 4, 8, and 40 kA/m were recently measured in similar particles[26] and were earlier proposed for Fe-MgO core−shell single magnetic domain nanoparticles with mean sizes in the range from 37 to 65 nm.[25]

For O18 colloids, increasing SAR_e behavior with increasing concentration is observed in the studied concentration range. A similar SAR dependence monotonously increasing with $[x]$ for an excitation field of 104 kHz and 32 kA/m has been reported for 22 nm DMSA-coated MNP.[47] A decreasing variation of SAR with respect to the nanoparticle concentrations was reported for well-dispersed 10 nm Fe_3O_4 MNP, uncoated and PAA coated, as well as for 100 nm composite nanospheres of polystyrene of the same MNPs embedded, as measured at ∼13 MHz and 4.5 kA/m.[31]

The observed SAR dependence on concentration suggests the use of concentration as a variable parameter to control dissipation at a fixed excitation field.

DOI: 10.1021/acs.langmuir.5b03559
Langmuir 2016, 32, 1201−1213

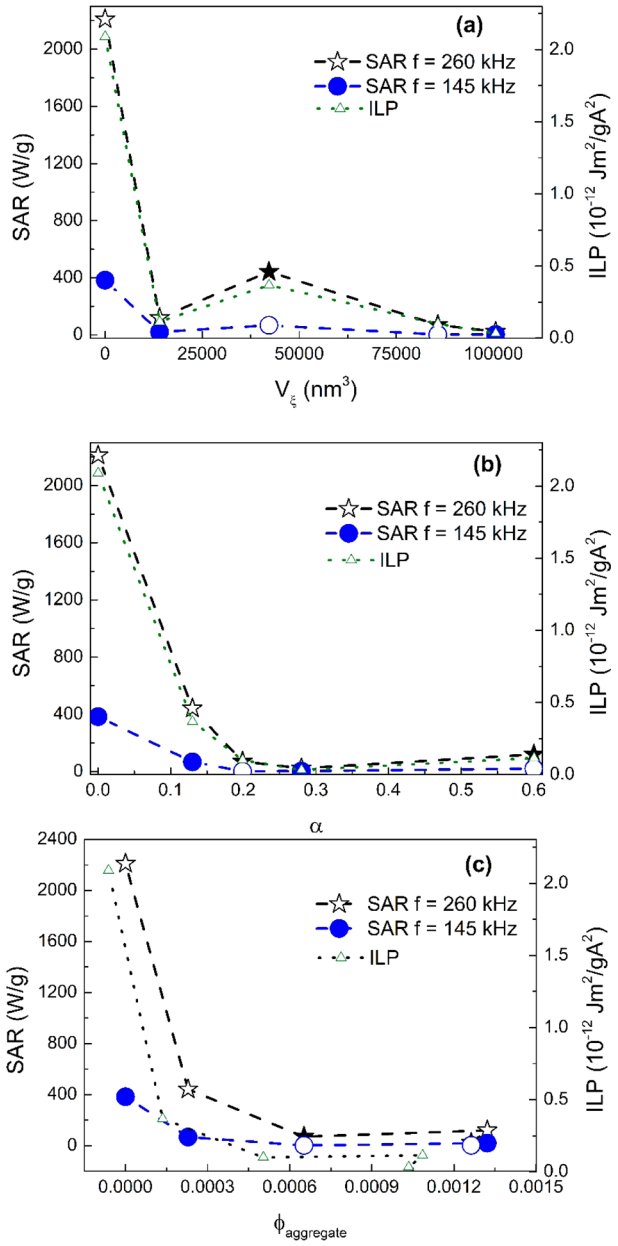

Figure 9. SAR and experimental ILP as a function of (a) cluster volume V_ξ, (b) particle fraction in nanoclusters α, and (c) volume fraction $\phi_{aggregated}$ of aggregated MNP. Closed symbols stand for experimental SARs values, and open symbols stand for extrapolated SARs values as explained in the text.

Numerical values for the frequency factor $\frac{\omega\tau}{1+\omega^2\tau^2}$ were derived from SAR_e, using eq 1, as

$$\frac{\omega\tau}{1+\omega^2\tau^2} \approx \beta\frac{6k_BT\rho}{\mu_0{}^2M_s{}^2VH_o{}^2\omega}SAR_e \quad (6)$$

with $\langle V\rangle$ being the MNP mean volume and β being a constant adjusted so that the frequency factor is equal to 0.5 at the maximum,[48] which occurs for $\omega\tau = 1$. This approximation holds for particles displaying a very low size dispersity. The thus-derived frequency factor was plotted against $[x]$ in Figure 10c with the corresponding relaxation times solved from eq 6.

We have analyzed the effects of interparticle interaction on SAR through a modification of the nanoparticle relaxation time using the analytical expression for the Néel relaxation time with the modification proposed by Landi:[28,29]

$$\tau_N = \tau_o \exp\left[\frac{KV}{k_BT} + 0.9\gamma\left(\frac{KV}{k_BT}\right)^2\right] \quad (7)$$

with $\gamma = \frac{N}{10}\left(\frac{\langle\mu^2\rangle\mu_o}{4\pi KV}\right)^2\left\langle\frac{1}{L^6}\right\rangle$, N being the total number of MNPs in the system, μ being the magnetic moment of the MNP, μ_o equal to $4\pi \times 10^{-7}$ H/m, and L being the interparticle distance. The relaxation time, as given by eq 7, was derived from a mean-field model where the dipolar interaction produced by a random spatial arrangement of MNPs was interpreted as a random field acting on a reference particle. In this calculation, the mean value of the random dipolar field contribution is null, irrespective of the magnetization values, so the second term in eq 7 comes from the second-order correction. A null mean value of a fluctuating dipolar field is valid only for an ensemble of monodisperse MNPs.

When bidisperse colloids are diluted, nanoclusters do not change their size, as established with SAXS measurements. Therefore, for MNPs belonging to nanoclusters, L in eq 7 remains constant and so do their SARs. However, mean interparticle distances of the single-MNP component depends on colloid concentration $[x]$ as $L = (\rho V/[x])^{1/3}$. Thus, SAR changes observed in Figure 10a,b can be due to an increase in interparticle distance (decrease in dipolar interaction) between non-nanoclustered MNPs and to a decrease in the total number of particles contributing to the fluctuating dipolar field with increasing dilution. Structural and magnetic parameters, listed in Tables 1 and 2 with K_{eff} retrieved from H_c vs T measurements, were again used to simulate SAR against colloid concentration considering the modified Néel relaxation time (eq 7). Simulations shown in Figure 10d corresponding to O18 and DMSA18 colloids are labeled as SAR_L. In the same figure, the concentration dependence of simulated relaxation times is plotted for both colloids. For the DMSA18 colloid, the crossover between τ_N and τ_B behaviors occurs at a concentration larger than the largest sample concentration, in agreement with the occurrence of the Néel mechanism over the whole studied colloid concentration range. For colloid O18, τ_B is smaller than τ_N, and there is no crossover indicating the occurrence of the Brown mechanism. Moreover, SAR_L calculated from K_{eff} values, measured in a frozen colloid and labeled as SAR_L O18 Néel in the figure, displays decreasing behavior with concentration, whereas SAR_L calculated by considering an effective relaxation time (within the assumption of independence between Brown and Néel phenomena), labeled as SAR_L O18, displays an increasing trend with concentration. The absence of a peak for sample O18 may be due to the occurrence of Brown instead of Néel relaxation.

It can be observed that the relaxation time as given by eq 7 depends on N, and then the power dissipated (P) by an ensemble of N particles becomes a nonextensive quantity. P as a function of N is not a homogeneous function of degree 1 as expected. This is a direct consequence of the long-range nature of the dipolar interaction. Due to the fact that all of the particles in the colloid contribute to the relaxation time of a given MNP as proposed in eq 7 but not with the same intensity, closer particles should have a stronger effect than those further away, we have used a value of $N = 5 \times 10^5$ for SAR_L. This N value is close to that used for a rough estimate of γ in ref 28.

DOI: 10.1021/acs.langmuir.5b03559
Langmuir 2016, 32, 1201−1213

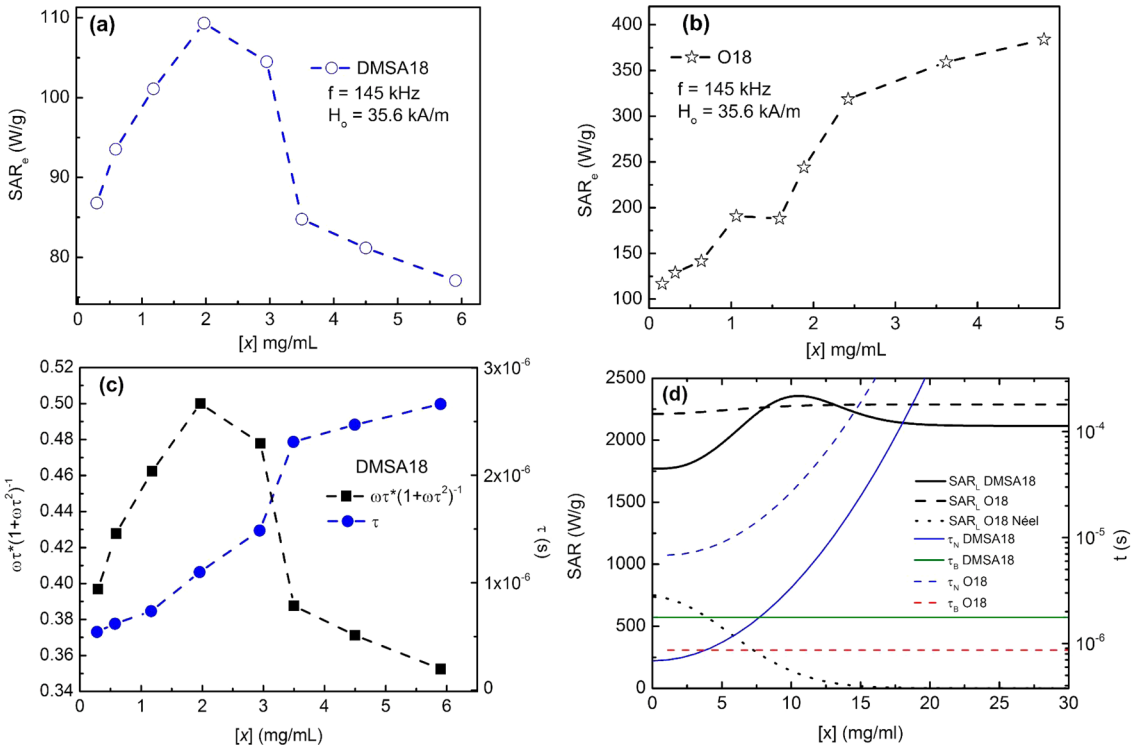

Figure 10. Experimental specific absorption rates SAR_e vs colloid concentration $[x]$ for (a) DMSA18 colloid and (b) O18 colloid. (c) Frequency factor and relaxation time τ calculated from SAR_e for DMSA18 colloid. (d) Brown (τ_B) and Néel (τ_N) relaxation time simulations for O18 and DMSA18 samples and SAR values simulated with eq 7 and replaced in eq 1 using K_{eff} listed in Table 2. SAR_LO18 Néel stands for simulation using only τ_N.

From the analysis with eq 7 of the experimental SAR, we conclude that the relaxation time as deduced by Landi[28] from the mean-field model under a random dipolar field approximation constitutes a theoretical improvement in the understanding of colloid SAR and in the development of analytical expressions for SAR data analysis. However, we believe that the τ dependence on N has to be revised because by using N as the total number of MNPs in the system relaxation time diverge. In the case of a long-range order interaction, all MNPs contribute, but eq 7 suggests that all MNPs contribute equally, which cannot be the case, and closer ones contribute more than far away ones. The SAR concentration (interparticle distance) dependence is experimentally verified, but SAR_e could not be quantitatively reproduced by replacing τ with the modified relaxation time (eq 7) in eq 1.

As already mentioned, a null mean value of a fluctuating dipolar field refers only to ensembles of monodisperse MNPs. Then the τ_N approximation given by eq 7 does not apply either to a colloid displaying a large size dispersion or to any MNPs configuration resulting in a static dipolar field. For these cases, the issue of SAR dependence on concentration is still an open question. We also point out that even for the Brown mechanism, magnetic interparticle interactions affect the magnetic-moment dynamics and thus the SAR in a nontrivial way that must be investigated in future work.

Our results demonstrating that nanoclustering highly reduces the SAR may help to understand the different characteristics of magnetic hyperthermia in in vitro and in vivo experiments. Notice that the endocytosis mechanism during MNPs' interaction with cells may induce clustering. Furthermore, the knowledge that power dissipated by well-dispersed MNPs is a nonextensive property would help to foresee changes in heat dissipation associated with variations in concentration after injection into living tissues. This effect should be properly taken into consideration for real therapeutic applications.

CONCLUSIONS

Magnetite nanoparticles, coated with oleic acid and subsequently modified with *meso*-2,3-dimercaptosuccinic acid to allow their aqueous suspension, were used to analyze the influence of aggregation and dipolar interactions on the specific absorption rate of bidisperse colloids. The studied colloids, based on 10 and 18 nm sizes, and two dispersions (oleic acid coated and dispersed in hexane and *meso*-2,3-dimercaptosuccinic acid coated and dispersed in water) are composed of stable nanoclusters coexisting with isolated nanoparticles. Both components dissipate heat under a radio frequency excitation in a distinctive way. It is shown that the nanoclustering of particles with randomly oriented easy axes is detrimental to the SAR. On the other hand, the contribution to SAR from individual nanoparticles determined for various colloid concentrations displays a peak for an 18 nm size aqueous suspension, i.e., SAR increases for increasing concentration, reaches a maximum, and then decreases for higher concentration. The power dissipated by an ensemble of randomly oriented magnetic nanoparticles became a nonextensive property. Then at a fixed field excitation parameter, the colloid concentration can be used to optimize the fluid SAR. Experimental SAR data could not be semiempirically reproduced with the analytical expression deduced from the linear response theory, using as input structural and magnetic properties measured with SAXS, TEM, and dc magnetometry. However, the tendency of colloids to exhibit higher SAR is reproduced when the single-particle relaxation time is modified (in order to account for dipolar

DOI: 10.1021/acs.langmuir.5b03559
Langmuir 2016, 32, 1201−1213

interactions among nanoparticles) following the expression derived by Landi[29] for a random dipolar-field approximation.

■ ASSOCIATED CONTENT

Supporting Information

The Supporting Information is available free of charge on the ACS Publications website at DOI: 10.1021/acs.langmuir.5b03559.

Additional material related to TEM, SAXS, magnetometry data (temperature coercive field dependence and IRM/DC), and relaxation times analysis. (PDF)

■ AUTHOR INFORMATION

Corresponding Author

*E-mail: raap@fisica.unlp.edu.ar.

Author Contributions

The manuscript was written through the contributions of all authors. All authors have given approval to the final version of the manuscript.

Notes

The authors declare no competing financial interest.

■ ACKNOWLEDGMENTS

We acknowledge CONICET and UNLP of Argentina for financial support with grants PIP 0720 and X11/680 and the European Union for Multifun (EU-FP ref 262943) and NanoMag (EU-FP7 ref 60448) projects and MAT2014-52069-R from the Spanish Ministry of Economy and Competitiveness. SAXS experiments were carried out at the D01B-SAXS beamline of Laboratorio Nacional de Luz Sincrotrón (Campinas-Brazil) under proposals D01B SAXS2-14429 and 16920. SAXS measurements against colloid concentration were carried out with the Bruker AXS-NanoStar camera at the Laboratorio de Crystalografía IF-USP (Sao Paulo-Brazil). M.B.F.v.R., P.M.Z., and F.H.S. are members of IFLP-CONICET, and D.F.C. is a postdoctoral fellow of CONICET.

■ REFERENCES

(1) Luo, S.; Wang, L. F.; Ding, W. J.; Wang, H.; Zhou, J. M.; Jin, H. K.; Su, S. F.; Ouyang, W. W. Clinical Trials of Magnetic Induction Hyperthermia for Treatment of Tumours. *OA Cancer* **2014**, *2* (1), 2.

(2) Maier-Hauff, K.; Ulrich, F.; Nestler, D.; Niehoff, H.; Wust, P.; Thiesen, B.; Orawa, H.; Budach, V.; Jordan, A. Efficacy And Safety Of Intratumoral Thermotherapy Using Magnetic Iron-Oxide Nanoparticles Combined With External Beam Radiotherapy On Patients With Recurrent Glioblastoma Multiforme. *J. Neuro-Oncol.* **2011**, *103* (2), 317−324.

(3) Carrey, J.; Mehdaoui, B.; Respaud, M. Simple Models For Dynamic Hysteresis Loop Calculations Of Magnetic Single-Domain Nanoparticles: Application To Magnetic Hyperthermia Optimization. *J. Appl. Phys.* **2011**, *109*, 083921.

(4) Usov, N. Low Frequency Hysteresis Loops Of Superparamagnetic Nanoparticles With Uniaxial Anisotropy. *J. Appl. Phys.* **2010**, *107*, 123909.

(5) Fernández van Raap, M. B.; Mendoza-Zelis, P.; Coral, D. F.; Torres, T. E.; Marquina, C.; Goya, G. F.; Sánchez, F. H. Self-organization in Oleic Acid-Coated $CoFe_2O_4$ Colloids: A SAXS Study. *J. Nanopart. Res.* **2012**, *14* (9), 1072−5.

(6) Wang, D.; Kowalczyk, B.; Lagzi, I.; Grzybowski, B. Bistability And Hysteresis During Aggregation Of Charged Nanoparticles. *J. Phys. Chem. Lett.* **2010**, *1* (9), 1459−1462.

(7) Palma, S. I. C. J.; Marciello, M.; Carvalho, A.; Veintemillas-Verdaguer, S.; Morales, M. P.; Roque, A. Effects Of Phase Transfer Ligands On Monodisperse Iron Oxide Magnetic Nanoparticles. *J. Colloid Interface Sci.* **2015**, *437*, 147−155.

(8) Kolosnjaj-Tabi, J.; Di Corato, R.; Lartigu, L.; Marangon, I.; Guardia, P.; Silva, A. K. A.; Luciani, N.; Clément, O.; Flaud, P.; Singh, J. V.; Dcuzzi, P.; Pellegrino, T.; Wilhelm, C.; Gazeau, F. Heat-Generating Iron Oxide Nanocubes: Subtle "Destructurators" Of The Tumoral Microenvironment. *ACS Nano* **2014**, *8* (5), 4268−4283.

(9) Wilhelm, C.; Gazeau, F. Universal Cell Labelling With Anionic Magnetic Nanoparticles. *Biomaterials* **2008**, *29* (22), 3161−3174.

(10) Billotey, C.; Wilhelm, C.; Devaud, M.; Bacri, J. C.; Bittoun, J.; Gazeau, F. Cell Internalization Of Anionic Maghemite Nanoparticles: Quantitative Effect On Magnetic Resonance Imaging. *Magn. Reson. Med.* **2003**, *49*, 646−654.

(11) Rosensweig, R. E. Heating Magnetic Fluid With Alternating Magnetic Field. *J. Magn. Magn. Mater.* **2002**, *252*, 370−374.

(12) Hergt, R.; Dutz, S.; Roder, M. Effects Of Size Distribution On Hysteresis Losses Of Magnetic Nanoparticles For Hyperthermia. *J. Phys.: Condens. Matter* **2008**, *20*, 385214.

(13) Klughertz, G.; Friedland, L.; Hervieux, P. A.; Manfredi, G. Autoresonant Switching Of The Magnetization In Single-Domain Nanoparticles: Two-Level Theory. *Phys. Rev. B: Condens. Matter Mater. Phys.* **2015**, *91*, 104433.

(14) Kallumadil, M.; Tada, M.; Nakagawa, T.; Abee, M.; Southern, P.; Pankhurst, Q. A. Suitability Of Commercial Colloids For Magnetic Hyperthermia. *J. Magn. Magn. Mater.* **2009**, *321* (10), 1509−1513.

(15) Roca, A. G.; Venitemillas-Verdaguer, S.; Port, M.; Robic, C.; Serna, C. J.; Morales, M. P. Effect of Nanoparticle and Aggregate Size on the Relaxometric Properties of MR Contrast Agents Based on High Quality Magnetite Nanoparticles. *J. Phys. Chem. B* **2009**, *113*, 7033−7039.

(16) Coral, D. F.; Mendoza Zélis, P.; de Sousa, M. E.; Muraca, D.; Lassalle, V.; Nicolás, P.; Ferreira, M. L.; Fernández van Raap, M. B. Quasi-Static Magnetic Measurements To Predict Specific Absorption Rates In Magnetic Fluid Hyperthermia Experiments. *J. Appl. Phys.* **2014**, *115*, 043907.

(17) Andreu, I.; Natividad, E.; Solozábal, L.; Roubeau, O. Nano-Objects For Addressing The Control Of Nanoparticle Arrangement And Performance In Magnetic Hyperthermia. *ACS Nano* **2015**, *9* (2), 1408−1419.

(18) Mehdaoui, B.; Tan, R. P.; Meffre, A.; Carrey, J.; Lachaize, S.; Chaudret, B.; Respaud, M. Increase of Magnetic Hyperthermia Efficiency Due to Dipolar Interactions in Low Anisotropy Magnetic Nanoparticles: Theoretical and Experimental Results. *Phys. Rev. B: Condens. Matter Mater. Phys.* **2013**, *87*, 174419.

(19) Jeun, M.; Bae, S.; Tomitaka, A.; Takemura, Y.; Ho Park, K.; Ha Paek, S.; Chung, K. W. Effects Of Particle Dipole Interaction On The AC Magnetically Induced Heating Characteristics Of Ferrite Nanoparticles For Hyperthermia. *Appl. Phys. Lett.* **2009**, *95*, 082501.

(20) Urtizberea, A.; Natividad, E.; Arizaga, A.; Castro, M.; Mediano, A. Specific Absorption Rates And Magnetic Properties Of Ferrofluids With Interaction Effects At Low Concentrations. *J. Phys. Chem. C* **2010**, *114* (11), 4916−4922.

(21) De la Presa, P.; Luengo, Y.; Velasco, V.; Morales, M. P.; Iglesias, M.; Veintemillas-Verdaguer, S.; Crespo, P.; Hernando, A. Particle Interactions in Liquid Magnetic Colloids by Zero Field Cooled Measurements: Effects on Heating Efficiency. *J. Phys. Chem. C* **2015**, *119*, 11022−11030.

(22) Hugounenq, P.; Levy, M.; Alloyeau, D.; Lartigue, L.; Dubois, E.; Cabuil, V.; Ricolleau, C.; Roux, S.; Wilhelm, C.; Gazeau, F.; Bazzi, R. Iron Oxide Monocrystalline Nanoflowers for Highly Efficient Magnetic Hyperthermia. *J. Phys. Chem. C* **2012**, *116*, 15702−15712.

(23) Deatsch, A. E.; Evans, B. A. Heating Efficiency In Magnetic Nanoparticle Hyperthermia. *J. Magn. Magn. Mater.* **2014**, *354*, 163−172.

(24) Sadat, M. E.; Patel, R.; Sookoor, J.; Bud'ko, S. L.; Ewing, R. C.; Zhang, J.; Xu, H.; Wang, Y.; Pauletti, G. M.; Mast, D. B.; Shi, D. Effect of spatial confinement on magnetic hyperthermia via dipolar interactions in Fe_3O_4 nanoparticles for biomedical applications. *Mater. Sci. Eng., C* **2014**, *42*, 52−63.

DOI: 10.1021/acs.langmuir.5b03559
Langmuir 2016, 32, 1201−1213

(25) Martinez-Buobeta, C.; Simeonidis, K.; Serantes, D.; Conde-Leborán, I.; Kazakis, I.; Stefanou, G.; Peña, L.; Galceran, R.; Balcells, L.; Monty, C.; Baldomir, D.; Mitrakas, M.; Angelakeris, M. Adjustable Hyperthermia Response of Self-Assembled Ferromagnetic Fe-MgO Core−Shell Nanoparticles by Tuning Dipole−Dipole Interactions. *Adv. Funct. Mater.* **2012**, *22* (17), 3737−3744.
(26) Conde-Leboran, I.; Baldomir, D.; Martinez-Boubeta, C.; Chubykalo-Fesenko, O.; Morales, M. P.; Salas, G.; Cabrera, D.; Camarero, J.; Teran, F.; Serantes, D. A Single Picture Explains Diversity of Hyperthermia Response of Magnetic Nanoparticles. *J. Phys. Chem. C* **2015**, *119* (27), 15698−15706.
(27) Dormann, J. L.; Bessais, L.; Fiorani, D. A Dynamic Study Of Small Interacting Particles: Superparamagnetic Model And Spin-Glass Laws. *J. Phys. C: Solid State Phys.* **1988**, *21*, 2015−2034.
(28) Landi, G. T. Role of Dipolar Interaction In Magnetic Hyperthermia. *Phys. Rev. B: Condens. Matter Mater. Phys.* **2014**, *89*, 014403.
(29) Landi, G. T. The Random Dipolar-Field Approximation For Systems Of Interacting Magnetic Particles. *J. Appl. Phys.* **2013**, *113*, 163908.
(30) Tan, R. P.; Carrey, J.; Respaud, M. Magnetic Hyperthermia Properties Of Nanoparticles Inside Lysosomes Using Kinetic Monte Carlo Simulations: Influence Of Key Parameters And Dipolar Interactions, And Evidence For Strong Spatial Variation Of Heating Power. *Phys. Rev. B: Condens. Matter Mater. Phys.* **2014**, *90*, 214421.
(31) Morales, M. B.; Phan, M. H.; Pal, S.; Frey, N. A.; Srikantha, H. Particle blocking and carrier fluid freezing effects on the magnetic properties of Fe_3O_4-based ferrofluids. *J. Appl. Phys.* **2009**, *105*, 07B511−3.
(32) Garcia-Otero, J.; Porto, M.; Rivas, J. Henkel Plots Of Single-Domain Ferromagnetic Particles. *J. Appl. Phys.* **2000**, *87*, 7376−7381.
(33) Salas, G.; Casado, C.; Terán, F. J.; Miranda, R.; Serna, C. J.; Morales, M. P. Controlled Synthesis Of Uniform Magnetite Nanocrystals With High-Quality Properties For Biomedical Applications. *J. Mater. Chem.* **2012**, *22*, 21065−21075.
(34) Salafranca, J.; Gazquez, J.; Pérez, N.; Labarta, A.; Pantelides, S. T.; Pennycook, S. J.; Batlle, X.; Varela, M. Surfactant Organic Molecules Restore Magnetism in Metal-Oxide Nanoparticle Surfaces. *Nano Lett.* **2012**, *12*, 2499−2503.
(35) Park, J.; An, K.; Hwang, Y.; Park, J. G.; Noh, H. J.; Kim, J.; Park, J. H.; Hwang, N. M.; Hyeon, T. Ultra-large-scale syntheses of monodisperse nanocrystals. *Nat. Mater.* **2004**, *3*, 891−895.
(36) Roca, A. G.; Marco, J. F.; Morales, M. P.; Serna, C. J. Effect of Nature and Particle Size on Properties of Uniform Magnetite and Maghemite Nanoparticles. *J. Phys. Chem. C* **2007**, *111*, 18577−18584.
(37) Freltoft, T.; Kjems, J. K.; Sinha, S. K. Power-Law Correlations And Finite-Size Effects In Silica Particle Aggregates Studied By Small-Angle Neutron Scattering. *Phys. Rev. B: Condens. Matter Mater. Phys.* **1986**, *33*, 269.
(38) Chen, S. H.; Teixeira, J. Structure and Fractal Dimension of Protein-Detergent Complexes. *Phys. Rev. Lett.* **1986**, *57*, 2583.
(39) Vargas, J. M.; Nunes, W. C.; Socolovsky, L. M.; Knobel, M.; Zanchet, D. Effect Of Dipolar Interaction Observed In Iron-Based Nanoparticles. *Phys. Rev. B: Condens. Matter Mater. Phys.* **2005**, *72*, 184428.
(40) Nunes, W. C.; Folly, W. S. D.; Sinnecker, J. P.; Novak, M. A. Temperature Dependence Of The Coercive Field In Single-Domain Particle Systems. *Phys. Rev. B: Condens. Matter Mater. Phys.* **2004**, *70*, 014419.
(41) Wohlfarth, E. P. Relations between Different Modes of Acquisition of the Remanent Magnetization of Ferromagnetic Particles. *J. Appl. Phys.* **1958**, *29*, 595−596.
(42) Kelly, P. E.; O'Grady, K.; Mayo, P. I.; Chantrell, R. W. Switching mechanisms in cobalt-phosphorus thin films. *IEEE Trans. Magn.* **1989**, *25* (5), 3881−3883.
(43) Curiale, J.; Sánchez, R. D.; Troiani, H. E.; Ramos, C. A.; Pastoriza, H.; Leyva, A. G.; Levy, P. Magnetism Of Manganite Nanotubes Constituted By Assembled Nanoparticles. *Phys. Rev. B: Condens. Matter Mater. Phys.* **2007**, *75*, 224410.
(44) Henkel, O. Remanenzverhalten und Wechselwirkungen in Hartmagnetischen Teilchenkollektiven. *Phys. Status Solidi B* **1964**, *7*, 919.
(45) Spratt, G. W. D.; Bissell, P. R.; Chantrell, R. W.; Wohlfarth, E. P. Static And Dynamic Experimental Studies Of Particulate Recording Media. *J. Magn. Magn. Mater.* **1988**, *75*, 309−318.
(46) Dymond, J. H.; Øye, H. A.H. A. Viscosity of Selected Liquid *n*-Alkanes. *J. Phys. Chem. Ref. Data* **1994**, *23*, 41−54.
(47) Salas, G.; Camarero, J.; Cabrera, D.; Takacs, H.; Varela, M.; Ludwing, R.; Teran, F. J. Modulation of Magnetic Heating via Dipolar Magnetic Interactions in Monodisperse and Crystalline Iron Oxide Nanoparticles. *J. Phys. Chem. C* **2014**, *118*, 19985−19994.
(48) Mendoza Zélis, P.; Pasquevich, G. A.; Stewart, S. J.; Fernández van Raap, M. B.; Aphesteguy, J.; Bruvera, I. J.; Laborde, C.; Pianciola, B.; Jacobo, S.; Sánchez, F. H. Structural And Magnetic Study Of Zinc-Doped Magnetite Nanoparticles And Ferrofluids For Hyperthermia Applications. *J. Phys. D: Appl. Phys.* **2013**, *46*, 125006−12.

DOI: 10.1021/acs.langmuir.5b03559
Langmuir 2016, 32, 1201−1213